OXFORD

*Carcinogenesis*, 2021, Vol. 42, No. 2, 232–242

**doi:10.1093/carcin/bgaa091**
Advance Access publication August 20, 2020
Original Article

ORIGINAL ARTICLE

# Targeting 14-3-3ε activates apoptotic signaling to prevent cutaneous squamous cell carcinoma

Thomas R.Holmes[1], Jenan Al Matouq[1,4], Matti Holmes[1], Natasha Sioda[1], Justin C.Rudd[1], Celia Bloom[1], Lauren Nicola[1], Nicholas Y.Palermo[2], Justin G.Madson[3], Sándor Lovas[1] and Laura A.Hansen[1,*]

[1]Department of Biomedical Sciences, Creighton University School of Medicine, 2500 California Pl, Omaha, NE 68178, USA, [2]Holland Computing Center, University of Nebraska–Lincoln, Lincoln, NE, USA and [3]Midwest Dermatology Clinic, Omaha, NE, USA [4]Present address: Mohammed Al-mana College for Medical Science, Dammam, Kingdom of Saudi Arabia

*To whom correspondence should be addressed. Tel: +1 402 280 4085; Fax: +1 402 280 2690; Email: LHansen@creighton.edu

## Abstract

More than a million cases of cutaneous squamous cell carcinoma are diagnosed in the USA each year, and its incidence is increasing. Most of these malignancies arise from premalignant lesions, providing an opportunity for intervention before malignant progression. We previously documented how cytoplasmic mislocalization of CDC25A in premalignant and malignant skin cancers confers resistance to apoptotic cell death via a mechanism that depends on its interaction with 14-3-3ε. From these data, we hypothesized that 14-3-3ε overexpression drives skin tumor development and progression, such that targeting 14-3-3ε may be a useful strategy for skin cancer treatment. Like CDC25A, 14-3-3ε was overexpressed and mislocalized to the cytoplasm of both benign and malignant human skin cancer. Skin-targeted deletion of the 14-3-3ε gene reduced skin tumor development by 75% and blocked malignant progression. 14-3-3ε suppressed apoptosis through activation of Akt, leading to inhibition of BCL2 associated agonist of cell death and upregulation of Survivin. Using virtual tetrapeptide libraries, we developed a novel peptide that specifically blocked 14-3-3ε heterodimerization and thereby prevented its interaction with CDC25A. The peptide reduced prosurvival signaling, killed skin cancer cells and reduced skin tumor growth in xenograft. Normal skin keratinocytes were unaffected by inhibition or deletion of 14-3-3ε. Thus, targeting of 14-3-3ε dimerization is a promising strategy for the treatment of premalignant skin lesions.

## Introduction

Non-melanoma skin cancer is the most prevalent malignancy in humans with cutaneous squamous cell carcinoma (SCC) accounting for >70% of all non-melanoma skin cancer–related deaths (1,2). Most of these SCC arise from premalignant precursors known as actinic keratoses (AKs), providing a unique opportunity for intervention before malignant progression (3). AKs often present as multiple lesions over a large region of skin, which makes surgical removal difficult. They also have a high rate of recurrence and progression to SCC, particularly in patients with multiple lesions (3). The best alternative to surgical intervention for AK is topical 5-fluorouracil, but it is ineffective in more than a quarter of patients and has adverse side effects (4). Thus, better targets and treatments are needed for premalignant and malignant non-melanoma skin cancer.

One such potential target is the family of 14-3-3 proteins, which consists of seven isoforms (β, ε, η, γ, σ, θ and ζ) that influence signaling pathways and cellular processes through their propensity to associate with a wide range of client proteins (5,6). 14-3-3 Proteins are active in either homodimeric or heterodimeric form, and individual monomers in dimers can bring their client proteins within close proximity, allowing effective interactions between two clients (7). As such, 14-3-3 proteins can function as oncogenes by promoting tumor-like characteristics such as cell survival, invasion and proliferation

**Received:** February 17, 2020; **Revised:** August 6, 2020; **Accepted:** August 13, 2020

**Abbreviations**

| | |
|---|---|
| SDK1 | sphingosine-dependent kinase-1 |
| SCC | squamous cell carcinoma |
| IC50 | half-maximal inhibitory concentration |
| WT | wild type |
| MT | mutant |
| DMBA | 7,12-dimethylbenz[a]anthracene |
| TPA | 12-O-tetradecanoylphorbol-13-acetate |
| MD | molecular dynamics |
| ANOVA | analysis of variance |

(8–10). We previously documented that interaction with 14-3-3 is required for CDC25A-mediated suppression of apoptosis in skin cancers (11). Herein we reveal 14-3-3ε as an essential CDC25A binding partner that activates prosurvival signaling and promotes skin cancer progression.

14-3-3ε has been implicated in many cancers including astrocytoma, hepatocellular carcinoma, colon cancer, meningioma, vulvar SCC, breast cancer, lung cancer and natural killer/T-cell lymphoma (9,10,12,13). 14-3-3ε inhibits apoptosis in osteosarcoma cells by suppressing transcription factor activity in the nucleus (14). Loss of 14-3-3ε increases apoptosis in response to stress in *Drosophila melanogaster* and chronic myelogenous leukemia cells, whereas overexpression of 14-3-3ε protected neuronal cells from apoptosis (15–17). A role for 14-3-3ε in resistance to ultraviolet irradiation-induced cell death has also been documented in a kidney cell culture model (18). These data suggest that 14-3-3ε may be a key anti-apoptotic regulator in skin cancer, which usually arise as a result of chronic ultraviolet exposure.

Because heterodimerization of 14-3-3ε with other 14-3-3 isoforms is required for its activity (19–21), we hypothesized that inhibition of 14-3-3ε dimerization may be a useful means to block its activity. Although inhibition of 14-3-3ε dimerization has not been reported, a strategy arising from the observation that dimerization of 14-3-3ζ is blocked by phosphorylation at Ser58 by sphingosine-dependent kinase-1 (SDK1) (22) was investigated. Woodcock *et al.* used a sphingosine-mimic to induce SDK1 activity, thereby increasing phospho-14-3-3ζ (P-Ser58), which led to increased apoptosis in leukemia cells (23). However, this method of indirectly targeting dimerization is immunosuppressive, and SDK1 phosphorylation of 14-3-3ε does not occur (22). Presently, no therapies exist to directly target dimerization of 14-3-3 proteins.

We hypothesized that targeting 14-3-3ε heterodimerization may be an effective strategy to reactivate proapoptotic pathways in premalignant lesions and prevent SCC development. In support of this hypothesis, we found that skin-targeted deletion of the 14-3-3ε gene substantially reduced skin tumor development and blocked malignant progression. 14-3-3ε suppressed apoptotic cell death in skin cancer cells by activating Akt, leading to inhibition of BCL2 associated agonist of cell death and upregulation of Survivin. Our *de novo* designed tetrapeptide blocked heterodimerization of 14-3-3ε with its preferential dimerization partners 14-3-3γ and -ζ to increase SCC apoptosis and reduce skin cancer growth. Normal skin cells with nuclear localization of 14-3-3ε were largely unaffected by targeting of 14-3-3ε. These data provide important proof-of-principle evidence for the potential of inhibition of 14-3-3ε activity for the treatment of skin cancer.

## Materials and methods

### Cell culture

Human skin SCC cell lines (SCC12B.2, SCC13, SRB12) were obtained from Dr. James Rheinwald and Dr. Tom Carey and authenticated as described in refs (24,25). Early passage and not immortalized normal human epidermal keratinocytes were obtained from Thermo Scientific, Waltham, MA. Cells were transfected with pcDNA3.1-HA-14-3-3ε (Addgene plasmid # 48797; http://n2t.net/addgene:48797;RRID:Addgene_48797) (26) or control plasmid or siRNA (4 siRNA sequences pooled) targeting 14-3-3ε (Dharmacon, Lafayette, CO), 14-3-3γ (Dharmacon), 14-3-3ζ (Dharmacon), Survivin (Cell Signaling, Danvers, MA), Akt (Dharmacon) or control siRNA (Santa Cruz Biotechnology, Dallas, TX), or treated with Akt inhibitor GSK690693 (Tocris Bioscience, Bristol, UK). Cells were treated with cycloheximide (100 μg/ml) (Abcam) 48 h after transfection or with fresh peptide daily for 48–96 h in Opti-MEM I Reduced Serum Medium (Invitrogen). Half-maximal inhibitory concentration ($IC_{50}$) was determined by treating with increasing concentrations of peptide (0–75 μM) in Opti MEM medium with reduced serum (Invitrogen) for four consecutive days. Neutral Red Cell Viability and Caspase-3/7 Glo (Promega Corporation, Madison, WI) assays were performed.

### Immunostaining, TUNEL and image analysis

Acquisition of human samples was part of a study approved by Creighton University's IRB. Otherwise discarded and excess tissues without patient identifiers were obtained. Immunostaining was performed using antibodies recognizing 14-3-3ε (Cell Signaling), 14-3-3γ (Cell Signaling), 14-3-3ζ (Cell Signaling), Survivin (Cell Signaling), P-Akt (S473) (Thermo Fisher), Keratin 5 (BioLegend, San Diego, CA), Keratin 1 (BioLegend), Keratin 6 (Biolegend), Loricrin (Novus Biologicals, Centennial, CO) or Ki67 (Abcam, Cambridge, UK). TUNEL (Terminal deoxynucleotidyl transferase dUTP nick end labeling) was carried out using Promega DeadEnd Fluorometric TUNEL system (Promega). Fluorescence intensity or the number of labeled cells was measured using an Olympus VS120 Slide Scanner (Olympus, Tokyo, Japan). Cellular localization of immunohistochemistry signal was determined in a double-blinded manner.

### Coimmunoprecipitation and immunoblotting

Coimmunoprecipitation was performed using Dynabeads Protein G Immunoprecipitation Kit (Life Technologies, Carlsbad, CA) after coupling with 14-3-3ε (Fisher Scientific, Waltham, MA) or Akt (Thermo Fisher) antibodies. Controls included immunoprecipitation reactions using IgG isotype control antibody and whole lysates. Antibodies recognizing 14-3-3ε, 14-3-3β, 14-3-3η, 14-3-3γ, 14-3-3σ, 14-3-3θ or 14-3-3ζ (Cell Signaling), P-Akt (S473) (Cell Signaling), total Akt (Cell Signaling), P-BAD (S136) (Cell Signaling), total BAD (Cell Signaling), Survivin (Cell Signaling), MSIN3A (Abcam), GAPDH (Abcam) or α/β-tubulin (Cell Signaling) were used for immunoblotting with a Chemidoc XRS Molecular Imager (Bio-Rad Laboratories, Hercules, CA).

### Animals

Groups of NCG mice (*NOD CRISPR Prkdc Il2r gamma/NjuCrl*) (Charles River, Malvern, PA) were injected s.c. with $5 \times 10^5$ SCC13 cells. Tumors (at 150 $mm^3$) were treated via intratumoral injection with vehicle or 2.5 nmol ES1P2 tetrapeptide daily for 2 days ($N = 3$) or every other day for 2 weeks ($N = 4$ for ES1P2 and $N = 5$ for vehicle) and then harvested for analysis 24 h after the last treatment. Conditional deletion of *Ywhae*, the gene for 14-3-3ε, in the epidermis was achieved by crossing 14-3-3$\varepsilon^{fl/+}$ C57Bl6 mice (27) with *KRT14-Cre recombinase* transgenic mice (28) on an FVB/N background and backcrossing for five generations on FVB/N mice. Male and female 14-3-3*fl/fl/Cre*$\varepsilon^{-}$ [wild type (WT)] and 14-3-3*fl/fl/Cre*$\varepsilon^{+}$ [mutant (MT)] mice ($N = 20$ WT, $N = 18$ MT) were topically treated with 50 nmol of 7,12-dimethylbenz[a]anthracene (DMBA) followed by topical 6.8 nmol of 12-O-tetradecanoylphorbol-13-acetate (TPA) (6.8 nmol) weekly for 5 weeks and then by twice weekly 6.8 nmol of TPA. Groups of mice were euthanized after 24, 27 or 30 weeks for histopathological characterization of all tumors by two board-certified dermatologists. All procedures were performed with the approval of and in accordance with the guidance of the Creighton University Institutional Animal Care and Use Committee. Animal protocols including this work were 690.4 (breeding), 809.3 (xenografts) and 842.3 (chemical carcinogenesis).

### Hras sequencing

Genomic DNA was extracted from FFPE tumors collected from 14-3-3 WT and MT animals following DMBA/TPA carcinogenesis using QIAamp

DNA FFPE Tissue Kit (Qiagen). Exon 2 of *Hras* was amplified via PCR using the following primer set: F 5′-GGTCAGGCATCTATTAGCCGTC; R 5′-GCCGAGACTCAACAGTGCGAG. Sanger sequencing of unpurified PCR products was performed by Genewiz (Genewiz, South Plainfield, NJ). Alternatively, following extraction from FFPE tumors, gDNA was sent to Genewiz for single-nucleotide polymorphism analysis at *Hras* codon 61.

### Tetrapeptide library

Three-dimensional structures for the virtual tetrapeptide library were generated using the YASARA program (29). The library contained all possible combinations of any standard amino acid residues, cysteine was excluded to prevent synthetic problems at later stage ($19^4$ = 130 321 structures). Four different terminal end protections were used: free, *N*-acetyl, C-terminal amide and both termini capped (4 × 130 321 = 521 284 structures). An in-house Python script automated peptide generation and minimization *in vacuo*. Minimization in solvent was unnecessary because the torsional angles are randomized during docking; only the bond lengths and angles needed correction after initial structure generation.

### Target selection and docking

The N-terminal region with residues Asp6, Tyr9 and Gln6 of 14-3-3ε, as unique residues among the seven isoforms of 14-3-3 proteins were identified as a binding site. The non-protein components in the X-ray structure of 14-3-3ε (PDB i.d. 3ual) (30) were deleted, and missing H-atoms were added using YASARA. The resultant structure was relaxed in an aqueous environment using 200 ns molecular dynamics (MD) simulation (see parameters below). Binding site residues were assigned using the ray-tracing algorithm included in the Molegro Virtual Docker program (31). All receptor grids were aligned to the geometric center of the identified binding sites and tetrapeptides were docked using the GPU screening module of Molegro Virtual Docker. Hits were clustered using Tabu clustering of Molegro Virtual Docker with root-mean square deviation cutoff of 2.5 Å, ensuring maximum diversity in poses. Poses were ranked according to their molegro-derived energies; this scoring function is a modified version of PLANTS and was considered optimal for protein-peptide docking.

### MD simulation

For the MD simulations, the GROMACS-2016 package (32) was used with the CHARMM36m force field (33). The structure of the 14-3-3-peptide complex was solvated in a dodecahedron with εTIP3P water molecules (34) and 0.15 M sodium chloride. The system was subjected to 1000 steps steepest descent energy minimization and then to 1 ns constant number of molecules, volume and temperature simulation at 300 K, so that the position of the protein-peptide complex was constrained at the center of the dodecahedron with a force constant of 1000 kJ/mol. The system was then equilibrated during a 10 ns unrestrained constant number of molecules, pressure and temperature (NPT) simulation at 1 bar pressure and 300 K temperature. The integration step was 2 fs, the LINCS algorithm (35) was used to constrain all bonds to their correct length with a warning angle of 30°. The protein-peptide complex and the solvent with ions were coupled to separate temperature baths with a relaxation constant of 0.1 ps. The peptide and the solvent with ions were coupled separately to constant pressure using method of Berendsen with a relaxation constant of 1.0 ps and 4.5 × $10^{-5}$/bar isothermal compressibility (36). The temperature was controlled by the stochastic velocity-rescaling method of Bussi *et al*. (37). The long-range electrostatic interactions were calculated using the particle mesh Ewald method with 1.2 nm cutoff distance applying Verlet scheme and 0.15 nm Fourier spacing. For the calculations of van der Waals interactions, the short-range and long-range cutoffs, respectively, were 1.0 and 1.2 nm using the force-switch modifier. Finally, 250 ns NPT simulation was performed at 300 K and 1 bar pressure. The parameters were the same as during equilibrations, except the protein-peptide complex and solvent with ions were separately coupled to a 1 bar Parrinello–Rahman barostat (38). After the initial 250 ns screening, those structures in which the peptides did not dissociate from the Tyr9 region of 14-3-3ε were further simulated for 2 μs using the same parameters as for the screening.

### Residue contribution binding energy

The residue contribution to the binding energy of peptides to 14-3-3ε for the last 50 ns of the 2 μs simulation was calculated using the g_mmpbsa software (39). For the calculations, solvent and solute dielectric constants were 80 and 4, respectively. Temperature and sodium chloride concentration were the same as in the simulations.

### Peptide production

Peptides were synthesized and purified to greater that 95% purity by Bachem Americas (Torrance, CA) and EZBiolabs (Carmel, IN).

### Statistical analysis

Comparisons between two groups were performed using a two-tailed Student's *t*-test, where $P \leq 0.05$. Significance was determined using one-way analysis of variance (ANOVA) with the Dunnett's *post hoc* test for comparison of more than two groups, where $P \leq 0.05$. For data collected at multiple time points, two-way ANOVA with a Bonferroni correction was used, where $P \leq 0.05$.

## Results

### Overexpressed cytoplasmic 14-3-3ε inhibits apoptosis in SCC cells

Immunohistochemical analysis revealed that 14-3-3ε expression was increased during skin cancer development and progression (Figure 1A). 14-3-3ε was detected primarily in the epidermis of normal skin and was localized to the nuclei of all epidermal cell layers (Figure 1A, left). 14-3-3ε immunostaining was increased in AK and SCC (Figure 1A, middle and right) and accompanied by a distinct shift from predominantly nuclear localization in normal skin to a more cytoplasmic pattern in tumors (Figure 1A and B). Similarly, increased expression of 14-3-3ε was seen in SCC versus normal human cell lines (Figure 1C).

To assess whether increased cytoplasmic 14-3-3ε suppressed apoptosis in SCC cells, 14-3-3ε was silenced (Figure 1E) or was transiently transfected (Figure 1F) in cutaneous SCC cell line SCC12B.2, which had elevated cytoplasmic 14-3-3ε similar to skin cancers (Figure 1C and D). Silencing of 14-3-3ε increased apoptosis by 65% (Figure 1G), whereas 14-3-3ε overexpression significantly decreased apoptosis (Figure 1H). Analysis of prosurvival pathways revealed regulation of several key signaling molecules in SCC cells. Levels of active Akt (P-S473) were reduced, inhibitory phosphorylation of BAD (S136) was increased and Survivin levels were decreased on silencing of 14-3-3ε (Figure 2A). Overexpression of 14-3-3ε had the opposite effect on Akt, BAD and Survivin (Figure 2B).

Because 14-3-3 proteins can protect client proteins from degradation [reviewed in ref. (40)], 14-3-3ε was silenced and the cells were treated with cycloheximide, revealing reduced stability of Akt upon abrogation of 14-3-3ε (Figure 2C). Immunoprecipitation of 14-3-3ε protein from SCC12B.2 cells confirmed its association with Akt (Figure 2D). Inhibitory phosphorylation of BAD at residue Ser136 was downstream of this interaction with Akt, as shown by the decrease in P-BAD after treatment with Akt inhibitor GSK690693 (Figure 2E). *Akt* silencing revealed that Survivin was similarly downstream of Akt (Figure 2F). The function of Survivin has been shown to be determined by its cellular localization. In the nucleus, Survivin is a mitotic regulator, and in the cytoplasm, it acts as a direct inhibitor of activated caspases (41,42). We postulated that 14-3-3ε may contribute to the accumulation of cytoplasmic Survivin in SCC cells. Silencing 14-3-3ε in SCC12B.2 cells reduced cytoplasmic Survivin while increasing nuclear Survivin (Figure 2G). Silencing of *Survivin* (Figure 2H) increased apoptosis in SCC12B.2 cells (Figure 2I). Thus, 4-3-3ε increased both the stability of Survivin and its cytoplasmic localization.

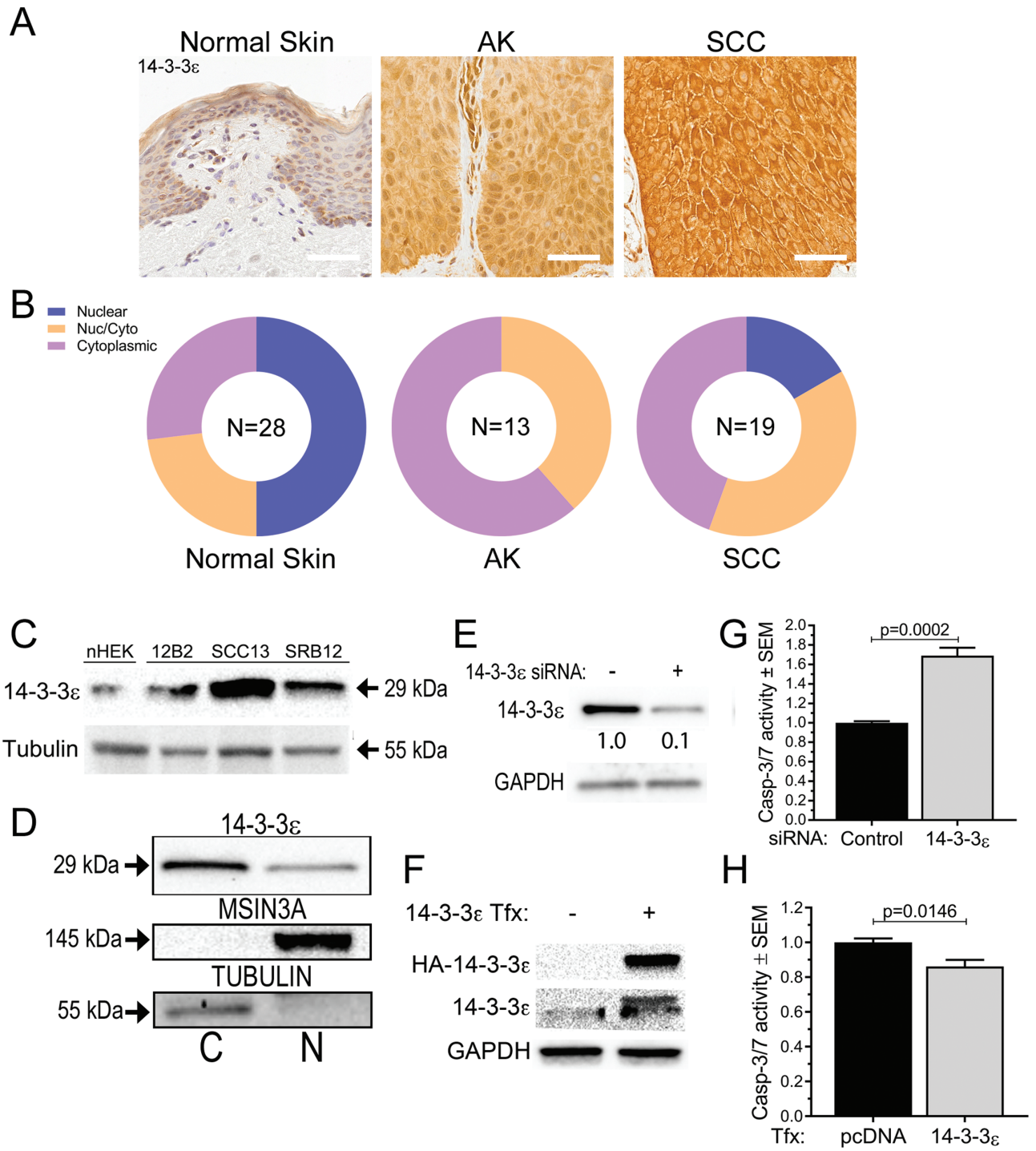


**Figure 1.** 14-3-3ε was overexpressed and shifted to the cytoplasm during SCC progression and inhibited apoptosis in SCC cells. (**A**) Immunohistochemistry for 14-3-3ε (brown) in human normal skin ($N = 28$), AK ($N = 13$) and SCC ($N = 19$) (scale bar = 50 μm). (**B**) Analysis of 14-3-3ε localization in normal, AK and SCC human skin was determined in a double-blinded manner; cytoplasmic represents more intense cytoplasmic versus nuclear intensity, cytoplasmic and nuclear (Cyto/Nuc) defined as equally intense in the nucleus and cytoplasm, nuclear was more intense nuclear versus cytoplasmic intensity. (**C**) 14-3-3ε levels in normal human epidermal keratinocytes (NHEK) and SCC lines SCC12B.2 (12B2), SCC13 and SRB12. (**D**) 14-3-3ε distribution in cytoplasmic (C) and nuclear (N) fractions from SCC12B.2 cells shown by immunoblotting. (**E–F**) Immunoblotting after silencing or transfection of 14-3-3ε in SCC12B.2 cells. (**G**) Apoptosis was measured using a Caspase-3/7 Glo assay in control siRNA or 14-3-3ε silenced SCC12B.2 cells 24 h after transfection ($N = 5$). (**H**) SCC12B.2 cells were transfected with 14-3-3ε or an empty vector and apoptosis was measured by a Caspase-3/7 Glo assay 24 h after transfection ($N = 5$). Significance was determined using a two-tailed Student's *t*-test, where $P \leq 0.05$ (G, H).

### 14-3-3ε-deficient skin was resistant to skin carcinogenesis

To assess the impact of 14-3-3ε on skin carcinogenesis *in vivo*, mice with skin-targeted deletion of the 14-3-3ε gene, *Ywhae*, were developed (Figure 3A and B). The skin of the 14-3-3ε MT mice had no obvious phenotype (Figure 3C and Supplementary Figure S1, available at *Carcinogenesis* Online). Following DMBA/TPA treatment, skin tumor numbers were suppressed by 75% in 14-3-3ε

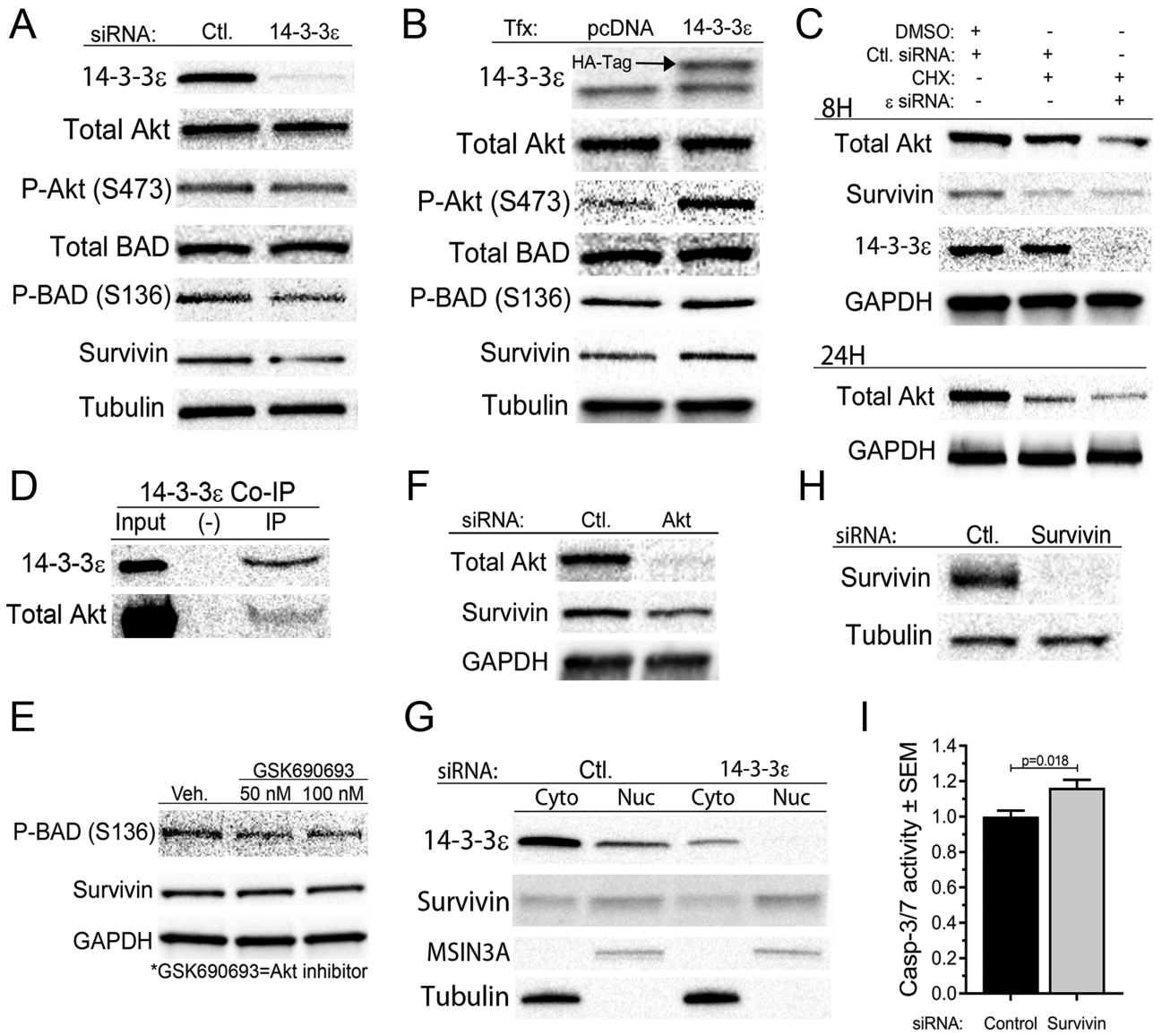


**Figure 2.** 14-3-3ε promoted SCC cell survival through P-Akt (S473)/P-BAD (S136)/Survivin signaling. SCC12B.2 cells were transfected with 14-3-3ε siRNA (**A**, **C**, **G**), *Akt* siRNA (**F**) or *Survivin* siRNA (**H, I**) for 48 h or with HA-tagged 14-3-3ε (**B**) for 24 h. SCC12B.2 cells were treated with either vehicle (DMSO), 50 nM or 100 nM Akt inhibitor GSK690693 (GSK) for 8 h (**E**) or with cycloheximide (CHX) for 8 or 24 h (**C**). (**D**) Immunoblotting (**A–C**, **E–H**) or coimmunoprecipitation of 14-3-3ε followed by immunoblotting (**D**) or Caspase-3/7 Glo Assay (**I**) is shown. MSIN3A and tubulin represent nuclear (nuc) and cytoplasmic (cyto) loading controls, respectively (**G**). Significance was determined using a two-tailed Student's *t*-test, $P \leq 0.05$ (**I**).

MT mice compared with controls (Figure 3D) with decreased tumor incidence as well (Figure 3E). Significantly, deletion of 14-3-3ε blocked progression to malignancy. Fifteen percent of the WT mice developed an SCC *in situ*, none of the 14-3-3ε-deficient mice did (Supplementary Figure S2A and B, available at *Carcinogenesis* Online). Of a small number of WT and MT tumors assessed, most sustained a mutation in codon 61 of *Hras* (Supplementary Figure S2C, available at *Carcinogenesis* Online).

### Development of inhibitors of 14-3-3ε heterodimerization for skin cancer treatment

The striking suppression of skin carcinogenesis upon 14-3-3ε deficiency suggests that it may be a useful target for treatment. Accordingly, we aimed to generate a novel and specific agent to inhibit 14-3-3ε. Because 14-3-3ε requires heterodimerization for its activity and the dimerization domain of 14-3-3 proteins contains the most heterogeneity of sequence (Figure 4A and B), we pursued a strategy to block 14-3-3ε dimerization. For this approach, we needed to decipher the heterodimerization patterns of 14-3-3ε with other 14-3-3 isoforms in skin cancer. Immunoprecipitation of 14-3-3ε in SCC cells revealed that 14-3-3ε dimerizes with 14-3-3γ or 14-3-3ζ in our SCC cells (Figure 5A). Both 14-3-3γ and -ζ exhibited predominantly nuclear localization in normal human skin with a shift to much more cytoplasmic localization in SCC (Figure 5B), consistent with the pattern seen for 14-3-3ε (Figure 2A and B). Similarly, there was a more cytoplasmic localization of 14-3-3 isoforms in multiple SCC cell lines and in mouse SCCs (data not shown). Silencing of 14-3-3γ or 14-3-3ζ in SCC cell lines also increased apoptosis (Figure 5C and D).

We aimed to develop a tetrapeptide to specifically target the N-terminal heterodimerization region of 14-3-3ε. The

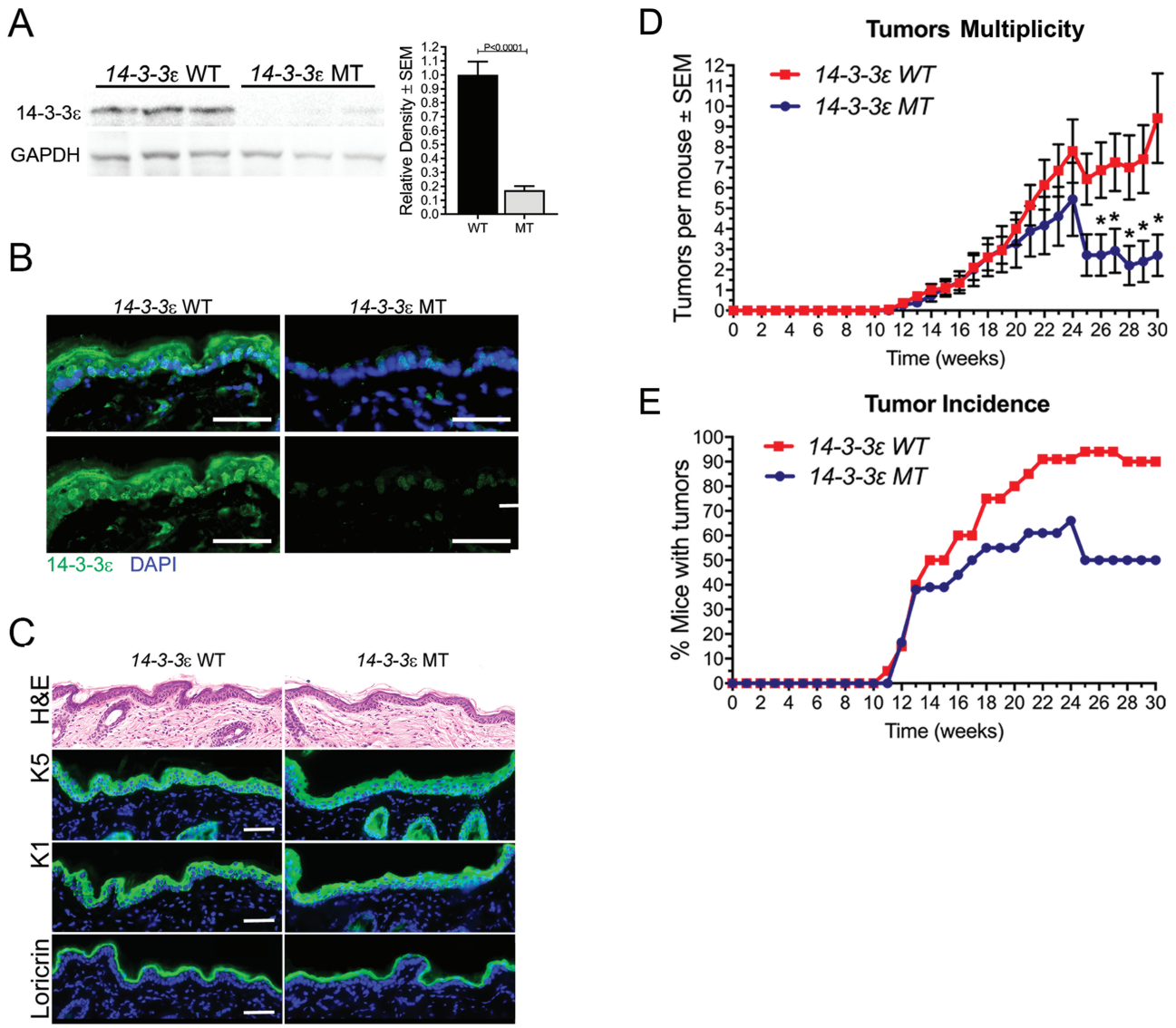


**Figure 3.** Deletion of 14-3-3ε did not disrupt normal skin but reduced tumorigenesis. (**A**) Immunoblot for 14-3-3ε in skin (left) and 14-3-3ε quantification normalized to GAPDH for N = 8 samples (right). Statistical significance was determined using a two-tailed Student's *t*-test, where $P \leq 0.05$. (**B**) Immunofluorescence on 14-3-3$^{fl/fl}$/*Cre*$^{-}$ (WT) and 14-3-3$^{fl/fl}$/*Cre*$^{+}$ (MT) skin for 14-3-3ε (FITC) with nuclei labeled by DAPI (blue) (scale bar = 50 μm). (**C**) H & E (top) or immunofluorescence of WT and MT mouse skin for keratin 5, keratin 1 and loricrin (scale bar = 50 μm). (**D**–**E**) Groups of male and female WT and MT mice were treated with DMBA and TPA for 24 (*N* = 4), 27 (*N* = 4) or 30 (*N* = 12 WT, *N* = 10 MT) weeks. Tumor multiplicity (D) and incidence (E). *Significance for tumor multiplicity using two-way ANOVA with Bonferroni correction, where *$P \leq 0.05$ (**D**).

aminoterminus of 14-3-3ε contains several unique residues (Asp6, Tyr9, Gln10) when compared with the other six 14-3-3 isoforms that could potentially allow for specific targeting (Figure 4A and B). Of the 521 284 structures in the virtual tetrapeptide library, 90 peptides docked favorably to the Tyr9 region of 14-3-3ε as assessed by the PLANTS scoring function of Molegro (Figure 4C). During 200 ns MD simulations of the selected 14-3-3-peptide complexes two peptides stayed bound to the N-terminus of ε14-3-3ε. The subsequent 2 μs MD simulation of the two complexes revealed that the novel tetrapeptide ES1P2 (Trp-Tyr-Trp-Lys-$NH_2$) still bound to the originally aimed N-terminal region of 14-3-3ε. Thus, it had the best potential for specifically targeting 14-3-3ε heterodimerization (Figure 4D). Root-mean-square deviation analysis of the 2 μs trajectory, using the backbone atoms, showed that ES1P2 dissociated from the N-terminus of 14-3-3ε at around 300 ns but remained bound to the region of residue 60–80. At 900 ns, the peptide moved back to the original N-terminal region of 14-3-3ε in a slightly different pose and stayed there for remainder of the MD simulation (Figure 4D). During the first phase (0–300 ns) of the MD simulation, N-terminal residues unique to the 14-3-3ε isoform (Asp6, Tyr9, Gln10, Glu25, Lys29 and Asp34) contributed to its association with ES1P2 (Figure 4E and F). In the third phase of MD simulation (900–2000 ns), when ES1P2 bound again to the N-terminal region of 14-3-3ε, residue contribution to binding was similar to that of the initial phase, except greater contribution from 14-3-3ε-specific residues Glu25 and Lys29 and less contribution from Asp6 were observed (Figure 4G and H). On the peptide side, Trp1 and Lys4 contributed most to its binding energy with 14-3-3ε.

## ES1P2 blocked 14-3-3ε dimerization and signaling, triggered SCC apoptosis and decreased SCC growth

The $IC_{50}$ of ES1P2 in cell survival assays of SCC12B.2 cells was 20.6 μM (Figure 6A) and treatment of SCC cells with ES1P2 significantly increased apoptosis (Figure 6B). ES1P2 at 20 μM partially

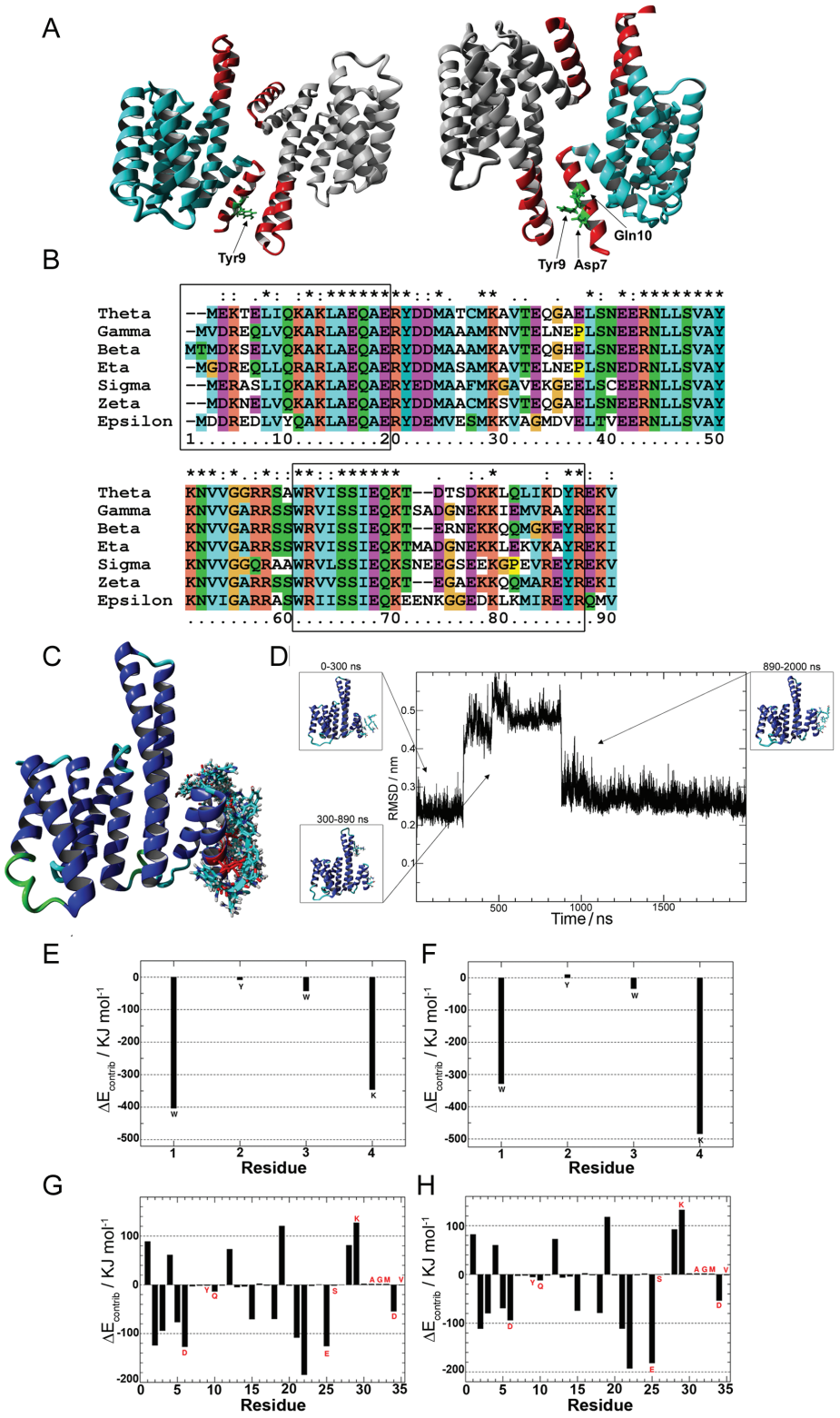


**Figure 4.** Heterodimeric structure of 14-3-3ε with the ζ isoform, sequence alignment of the first 90 residues of the seven isoforms, and specific targeting of 14-3-3ε heterodimerization with the novel peptide ES1P2. (**A**) In the heterodimer, ε is in cyan and ζ in gray color. Residues 1–18 and 60–87 of the dimerization domains are highlighted in red. Unique residues (Asp6, Tyr9 and Gln10) of the ε isoform are in green. Left is the front and the 180 degrees rotated structure is on right. (**B**) Amino acid sequences for the seven 14-3-3 isoforms from residues 1 to 90. '*', conserved residues among all seven isoforms; ':', conservative mutations; '•' semi-conservative mutations; no symbol, non-conservative mutations. Heterodimerization domains are marked with a box. (**C**) Of the 521 284 structures in the virtual tetrapeptide library, 90 peptides docked favorably to the N-terminal dimerization domain of 14-3-3ε (red color). On the basis of 200 ns MD simulations of the 14-3-3-peptide complexes, εES1P2 was chosen for detailed MD analysis. (**D**) Root-mean square deviation analysis of the 2 μs trajectory of the 14-3-3ε–ES1P2 complex indicates that the peptide interacted most of the simulation time with the N-terminal dimerization domain of 14-3-3ε. Between 300 and 900 ns, the peptide bound to residues 60–80 of 14-3-3ε, but after 900 ns, it remained closely bound again to the N-terminal region. (**E**–**H**) Residue contributions to binding energy during the initial 300 ns (E, F) and the last 1100 ns (G, H) phases of the simulation. ES1P2 on top and the N-terminal region of 14-3-3ε on bottom. Red colored letters indicate unique residues in 14-3-3ε.

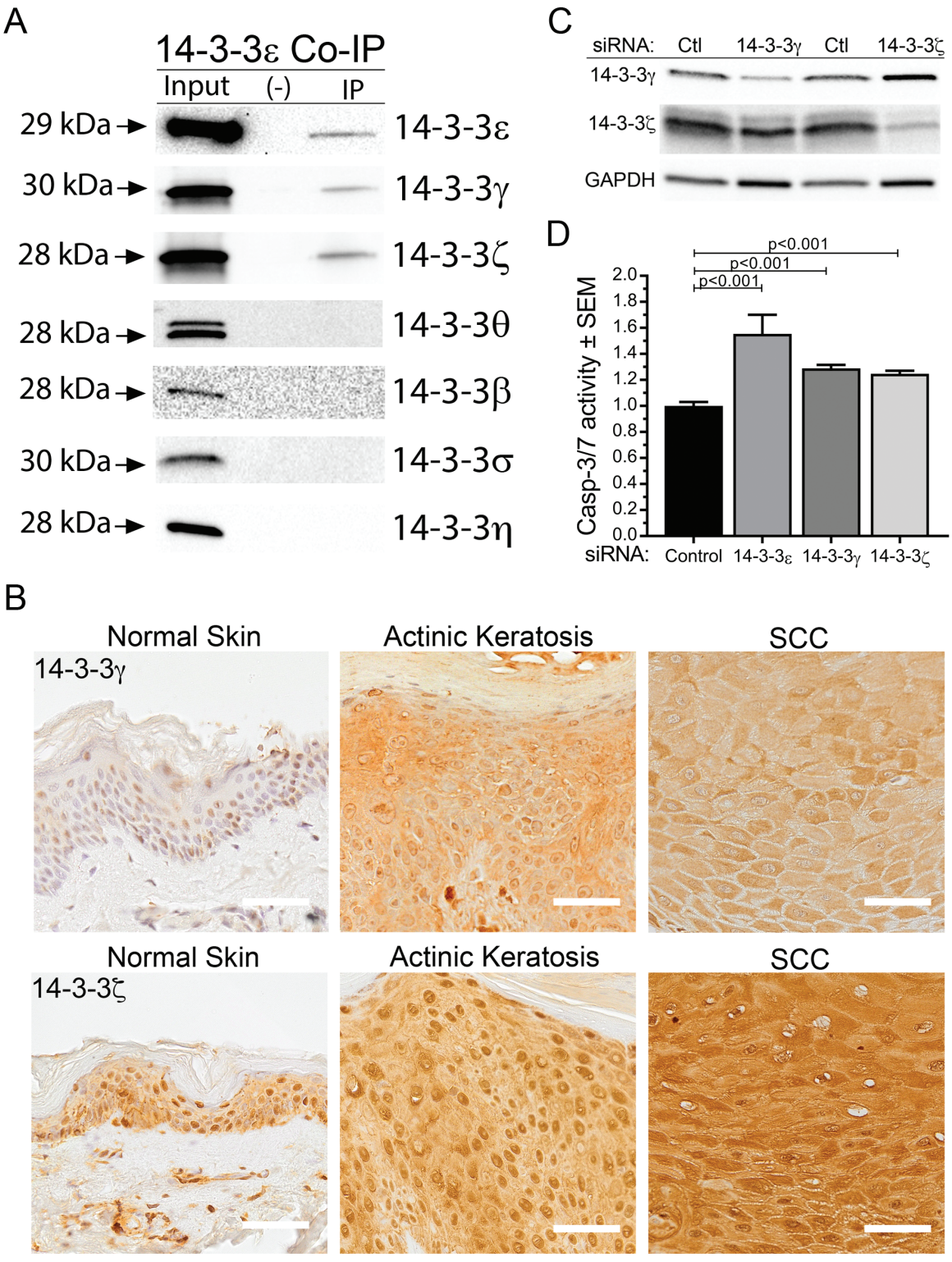


**Figure 5.** 14-3-3ε formed heterodimers with 14-3-3γ and 14-3-3ζ, which were relocalized from the nucleus to the cytoplasm in human SCC and inhibited apoptosis in SCC cells. (**A**) Immunoprecipitated 14-3-3ε protein isolated from 100 mg of SCC12B.2 cells analyzed by immunoblot. (**B**) Immunohistochemistry in human normal skin, AK and SCC sections for 14-3-3γ or 14-3-3ζ ($N \geq 6$) (scale bar = 50 μm). (**C**) Immunoblot of SCC12B.2 cell lysates from cells treated with control (Ctl) siRNA or siRNA targeting 14-3-3γ or 14-3-3ζ for 48 h. (**D**) Caspase-3/7 Glo assay 48 h after 14-3-3ε, 14-3-3γ or 14-3-3ζ silencing in SCC12B.2 cells. Significance determined using one-way ANOVA followed by Dunnett's *post hoc* test, $P \leq 0.05$ (D).

blocked 14-3-3ε association with 14-3-3γ and 14-3-3ζ (Figure 6C). In contrast, and as expected given the altered localization of 14-3-3ε in SCC compared with normal skin, as well as the lack of phenotype in 14-3-3ε MT mouse skin, ES1P2 was nontoxic to normal keratinocytes (Figure 6A, dashed line). Xenografts of human skin SCC cells were treated intratumorally with ES1P2, revealing a doubling of TUNEL-positive SCC cells (Figure 6D). In addition, ES1P2 decreased P-Akt (S473) (Figure 6E) and Survivin

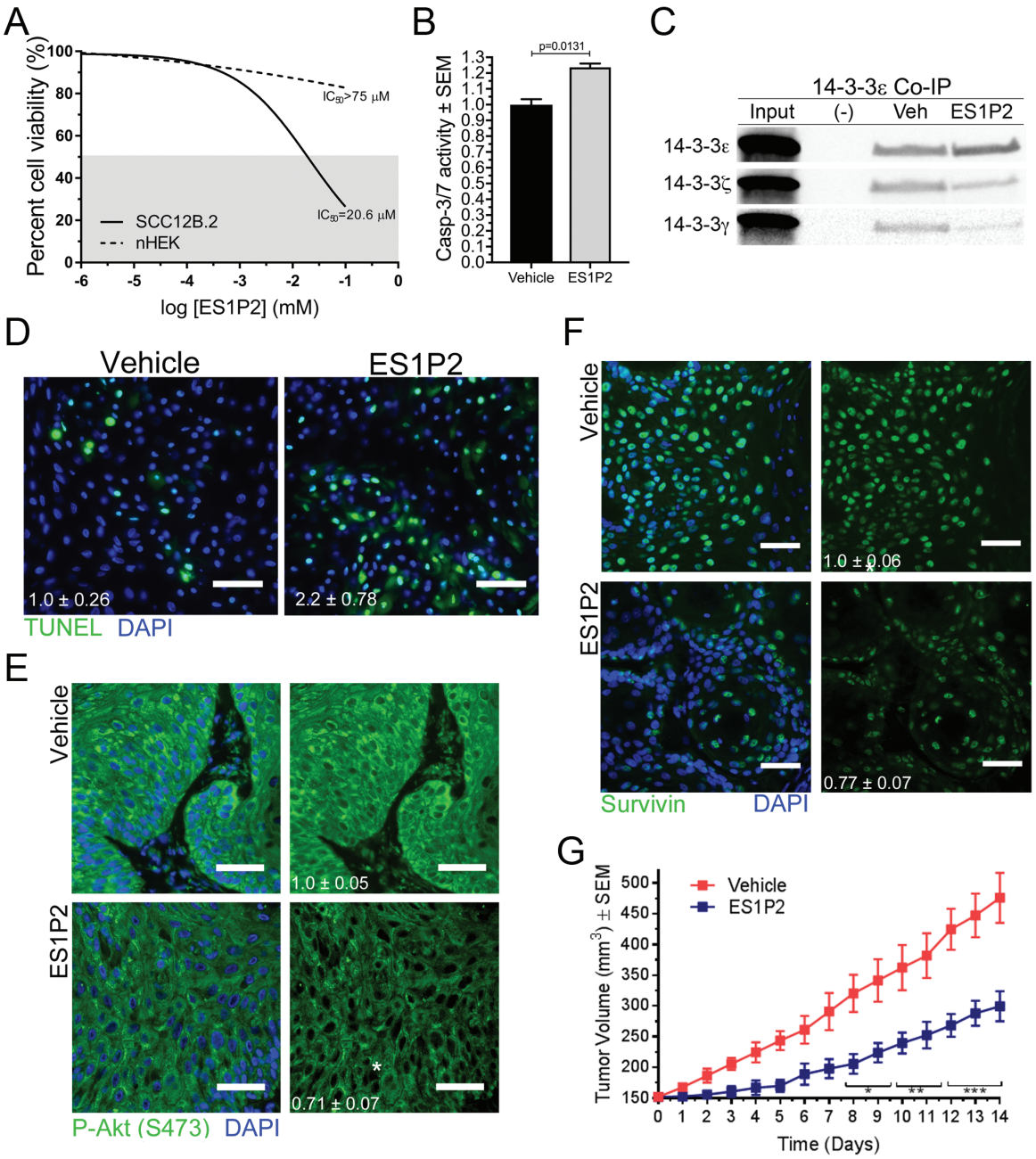


**Figure 6.** Treatment of SCC cells with tetrapeptide ES1P2 reduced 14-3-3ε heterodimerization, increased apoptosis and suppressed tumor growth. (**A**) $IC_{50}$ of ES1P2 in SCC12B.2 and NHEK cells using increasing concentrations of peptide ranging from 0 to 75 μM in neutral red cell viability assays. The dotted line indicates 50% survival threshold. Graphs represent the average $IC_{50}$ from three biological replicates with each treatment condition having four technical replicates ($N = 12$). (**B**) Apoptosis assessed in SCC12B.2 cells treated with vehicle or ES1P2 (20 μM) for 24 h followed by a Caspase-3/7 Glo assay ($N = 5$). (**C**) Immunoprecipitated 14-3-3ε protein from SCC12B.2 cells treated with vehicle (Veh) or ES1P2 (20 μM) for 48 h; (–) control using equal number of cells incubated with IgG isotype control antibody; images are representative of two separate experiments. (**D–G**) Xenografts of SCC cells were treated with ES1P2 or vehicle daily for 2 days (D–F) ($N = 3$ mice/group) or 3×/week for 2 weeks (G) ($N \geq 4$ mice/group) and killed the next day for TUNEL (D) and immunofluorescence analysis (E–F) or assessment of tumor growth (G). The white font indicates the number of apoptotic cells per $\mu m^2$ ± SEM relative to vehicle (D) or the relative immunofluorescence intensity ± SEM for all three tumors (E–F). All images are representative of three biological replicates ($N = 3$). Significance determined using a two-tailed Student's *t*-test (B, D–F) or two-way ANOVA (G). $^*P \leq 0.05$, $^{**}P \leq 0.01$, $^{***}P \leq 0.001$, respectively.

(Figure 6F) levels in SCC, consistent with the effects of 14-3-3ε silencing (Figure 2A). ES1P2 treatment reduced SCC growth in xenograft by half (Figure 6G).

## Discussion

Following our previous observations of CDC25A binding to cytoplasmic 14-3-3 to provide tumor-specific mechanisms to bypass apoptosis (11), we demonstrated the biological contribution of 14-3-3ε to skin cancer and the mechanisms by which 14-3-3ε acts. 14-3-3ε was increased and relocalized from the nucleus to the cytoplasm during skin cancer development and progression. Once in the cytoplasm it activated prosurvival signaling through P-Akt (Ser473), P-BAD (S136) and Survivin to facilitate skin carcinogenesis. Consistent with the ability of 14-3-3ε to promote cytoplasmic sequestration of client proteins, 14-3-3ε relocalized Survivin to the cytoplasm, a localization pattern that is closely tied to the anti-apoptotic function of Survivin

(41,42). Conditional deletion of the gene for 14-3-3ε substantially reduced skin tumor development and blocked progression to malignancy. Interestingly, tumors that developed in 14-3-3ε-deficient skin were found to have a similar incidence of *Hras* mutation to those that developed in normal skin. This suggests that abberant Hras activation is probably still a key driver of DMBA/TPA induced skin tumorigenesis in the absence of 14-3-3ε expression. These features, and the lack of effect of 14-3-3ε ablation on normal skin, made 14-3-3ε a particularly appealing target for treatment. Our novel tetrapeptide ES1P2 reduced 14-3-3ε heterodimerization, killed SCC cells but not normal keratinocytes, and decreased tumor growth. Taken together, these data document both an important role for 14-3-3ε in imparting cancer cells with resistance to apoptosis and a strategy for inhibiting 14-3-3ε to prevent skin carcinogenesis.

Because Akt/phosphoinositide 3-kinase signaling pathways can directly influence Survivin protein and transcripts (43,44), we propose that the effect of 14-3-3ε on Survivin may be linked to its direct stabilization of Akt. Similar to what we observed with the ability of 14-3-3ε to stabilize Akt, Kohama *et al*. demonstrated that 14-3-3ε protects CDC25A from ubiquitin-mediated degradation in HeLa cells (45).

Herein we targeted the function of 14-3-3ε by directly blocking its ability to form dimers. Despite the propensity and necessity of 14-3-3 dimer formation for their function, the development of therapeutics aimed at inhibition of dimer formation has not been fully explored. 14-3-3 Dimers were indirectly targeted in leukemia cells by inducing the SDK1 phosphorylation of Ser58 on 14-3-3ζ, a modification that prevents 14-3-3ζ dimerization (23). Other than in 14-3-3ζ, phospho-Ser has only been shown in 14-3-3β (Ser60) and in 14-3-3η (Ser59) (22). 14-3-3 Proteins have high sequence variation on their N-terminal dimerization domain, so we took an approach of developing a short peptide that preferentially binds to the N-terminal residues unique to 14-3-3ε. Our *de novo* designed peptide, ES1P2 is more effective at killing SCC cells than 5-fluorouracil, the most effective approved therapy for premalignant skin cancers. Furthermore, our peptide avoided toxicity to normal skin or skin cells in culture, suggesting minimal side effects with topical use clinically. Future work will focus on developing second generation peptides to induce a more robust effect on SCC cell viability.

We found that 14-3-3ε formed dimers with either 14-3-3γ and 14-3-3ζ. The pattern of 14-3-3ε, -γ and -ζ heterodimerization in SCC cells may have implications for cancer cell resistance to chemotherapy. Of the seven 14-3-3 isoforms, ε, γ and ζ are the ones most often associated with chemoresistance in various cancers [reviewed in ref. (46)]. For example, in breast cancer cells overexpression of 14-3-3ζ leads to resistance to anthracycline treatment, 14-3-3γ is often overexpressed in chemoresistant melanoma cells, and T-cell lymphoma expressing high levels of 14-3-3ε is resistant to adriamycin and vindesine (12,47–49). Whether a similar mechanism is at play in cutaneous SCC is yet to be determined, but due to the increased aggressiveness of reoccurring SCCs, development of therapeutics to target 14-3-3 protein dimerization, as we have done with ES1P2, may prove to be beneficial for reoccurring skin tumors. These data suggest that targeting 14-3-3ε function and its ability to form dimers has significant potential as a therapeutic strategy for the prevention and treatment of skin cancer.

## Supplementary material

Supplementary data are available at *Carcinogenesis* online.

Figure S1. **Deletion of 14-3-3ε did not induce a stress response in normal epidermis. A)** Keratin 6 (FITC) immunofluorescence (top panels) and hematoxylin and eosin staining (bottom panels) on *14-3-3fl/fl/Cre*$^{-}$ (WT) and *14-3-3fl/fl/Cre*$^{+}$ (MT) skin. Images were captured at 20x magnification.

Figure S2. **Histological grading of lesions resulting from DMBA/TPA tumorigenesis. A)** H & E of representative sections of a benign tumor (seborrheic keratosis) from each group and a SCC *in situ* (SCC) from WT (scale bar = 200 μm, top and 500 μm bottom). **B)** Number and proportion (%) of total (N) mice bearing a SCC *in situ*. **C)** Proportion of DMBA/TPA derived tumors from *14-3-3fl/fl/Cre*$^{-}$ (WT) and *14-3-3fl/fl/Cre*$^{+}$ (MT) mice harboring the *Hras*$^{CAA61CTA}$ mutation. Representative Sanger sequencing traces of heterozygous *Hras* mutant tumors shown below, substitution denoted by red asterisk.

## Funding

This research was supported by grants to LAH and SL from the State of Nebraska Cancer and Smoking-related Diseases Research Program and the National Institutes of Health (grant no. 1 R01 CA253573-01). The authors have applied for a patent on the peptides described herein. The authors have no other conflict of interest to declare.

## Acknowledgements

We appreciate the assistance of Toni Howard of the Creighton University Histology Core Facility. This research was supported by revenue from Nebraska's excise tax on cigarettes awarded to LAH through the Nebraska Department of Health and Human Services (DHHS). The authors have applied for a patent on the peptides described herein. Its contents represent the views of the authors and do not necessarily represent the official views of the State of Nebraska or DHHS.

*Conflict of Interest Statement*: None declared.

## References

1. Thompson, A.K. *et al.* (2016) Risk factors for cutaneous squamous cell carcinoma recurrence, metastasis, and disease-specific death: a systematic review and meta-analysis. *JAMA Dermatol.*, 152, 419–428.
2. Alam, M. *et al.* (2001) Cutaneous squamous-cell carcinoma. *N. Engl. J. Med.*, 344, 975–983.
3. Feldman, S.R. *et al.* (2011) Progression of actinic keratosis to squamous cell carcinoma revisited: clinical and treatment implications. *Cutis*, 87, 201–207.
4. Jansen, M.H.E. *et al.* (2019) Randomized trial of four treatment approaches for actinic keratosis. *N. Engl. J. Med.*, 380, 935–946.
5. Yaffe, M.B. *et al.* (1997) The structural basis for 14-3-3:phosphopeptide binding specificity. *Cell*, 91, 961–971.
6. Muslin, A.J. *et al.* (1996) Interaction of 14-3-3 with signaling proteins is mediated by the recognition of phosphoserine. *Cell*, 84, 889–897.
7. Gardino, A.K. *et al.* (2006) Structural determinants of 14-3-3 binding specificities and regulation of subcellular localization of 14-3-3-ligand complexes: a comparison of the X-ray crystal structures of all human 14-3-3 isoforms. *Semin. Cancer Biol.*, 16, 173–182.
8. Masters, S.C. *et al.* (2001) 14-3-3 proteins mediate an essential anti-apoptotic signal. *J. Biol. Chem.*, 276, 45193–45200.
9. Khorrami, A. *et al.* (2017) The functional significance of 14-3-3 proteins in cancer: focus on lung cancer. *Horm. Mol. Biol. Clin. Investig.*, 32.
10. Liu, Y. *et al.* (2012) Triptolide inhibits colon cancer cell proliferation and induces cleavage and translocation of 14-3-3 epsilon. *Cell Biochem. Funct.*, 30, 271–278.
11. Al-Matouq, J. *et al.* (2017) Accumulation of cytoplasmic CDC25A in cutaneous squamous cell carcinoma leads to a dependency on CDC25A for cancer cell survival and tumor growth. *Cancer Lett.*, 410, 41–49.

12. Qiu, Y. *et al.* (2017) Pretreatment 14-3-3 epsilon level is predictive for advanced extranodal NK/T cell lymphoma therapeutic response to asparaginase-based chemotherapy. *Proteomics Clin. Appl.*, 11, 3–4.
13. Liu, T.A. *et al.* (2013) 14-3-3epsilon overexpression contributes to epithelial-mesenchymal transition of hepatocellular carcinoma. *PLoS One*, 8, e57968.
14. Lu, K *et al.* (2018) 14-3-3epsilon is a nuclear matrix protein, and its altered expression and localization are associated with curcumin-induced apoptosis of MG-63 cells. *Oncol. Lett.*, 15, 338–346.
15. Kuzelová, K. *et al.* (2009) Isoform-specific cleavage of 14-3-3 proteins in apoptotic JURL-MK1 cells. *J. Cell. Biochem.*, 106, 673–681.
16. Nielsen, M.D. *et al.* (2008) 14-3-3 Epsilon antagonizes FoxO to control growth, apoptosis and longevity in Drosophila. *Aging Cell*, 7, 688–699.
17. Wu, J.S. *et al.* (2009) Ligand-activated peroxisome proliferator-activated receptor-gamma protects against ischemic cerebral infarction and neuronal apoptosis by 14-3-3 epsilon upregulation. *Circulation*, 119, 1124–1134.
18. Han, D. *et al.* (2010) Functional identification of a novel 14-3-3 epsilon splicing variant suggests dimerization is not necessary for 14-3-3 epsilon to inhibit UV-induced apoptosis. *Biochem. Biophys. Res. Commun.*, 396, 401–406.
19. Chaudhri, M. *et al.* (2003) Mammalian and yeast 14-3-3 isoforms form distinct patterns of dimers *in vivo*. *Biochem. Biophys. Res. Commun.*, 300, 679–685.
20. Yang, X. *et al.* (2006) Structural basis for protein–protein interactions in the 14-3-3 protein family. *Proc. Natl Acad. Sci. USA*, 103, 17237–17242.
21. Messaritou, G. *et al.* (2010) Dimerization is essential for 14-3-3zeta stability and function *in vivo*. *J. Biol. Chem.*, 285, 1692–1700.
22. Megidish, T. *et al.* (1998) A novel sphingosine-dependent protein kinase (SDK1) specifically phosphorylates certain isoforms of 14-3-3 protein. *J. Biol. Chem.*, 273, 21834–21845.
23. Woodcock, J.M. *et al.* (2015) Destabilisation of dimeric 14-3-3 proteins as a novel approach to anti-cancer therapeutics. *Oncotarget*, 6, 14522–14536.
24. Zhao, M. *et al.* (2011) Assembly and initial characterization of a panel of 85 genomically validated cell lines from diverse head and neck tumor sites. *Clin. Cancer Res.*, 17, 7248–7264.
25. Rheinwald, J.G. *et al.* (1981) Tumorigenic keratinocyte lines requiring anchorage and fibroblast support cultured from human squamous cell carcinomas. *Cancer Res.*, 41, 1657–1663.
26. Chen, H.K. *et al.* (2003) Interaction of Akt-phosphorylated ataxin-1 with 14-3-3 mediates neurodegeneration in spinocerebellar ataxia type 1. *Cell*, 113, 457–468.
27 Toyo-oka, K. *et al.* (2014) 14-3-3epsilon and zeta regulate neurogenesis and differentiation of neuronal progenitor cells in the developing brain. *J. Neurosci.*, 34, 12168–12181.
28. Hafner, M. *et al.* (2004) Keratin 14 Cre transgenic mice authenticate keratin 14 as an oocyte-expressed protein. *Genesis*, 38, 176–181.
29. Krieger, E. *et al.* (2015) New ways to boost molecular dynamics simulations. *J. Comput. Chem.*, 36, 996–1007.
30. Molzan, M. *et al.* (2012) Structural insights of the MLF1/14-3-3 interaction. *FEBS J.*, 279, 563–571.
31. Thomsen, R. *et al.* (2006) MolDock: a new technique for high-accuracy molecular docking. *J. Med. Chem.*, 49, 3315–3321.
32. Kutzner, C. *et al.* (2015) Best bang for your buck: GPU nodes for GROMACS biomolecular simulations. *J. Comput. Chem.*, 36, 1990–2008.
33. Huang, J. *et al.* (2017) CHARMM36m: an improved force field for folded and intrinsically disordered proteins. *Nat. Methods*, 14, 71–73.
34 Jorgensen, W. *et al.* (1983) Comparison of simple potential functions for simulating liquid water. *J. Chem. Phys.*, 79, 926–935.
35 Hess, B. *et al.* (1997) LINCS: a linear constraint solver for molecular simulations. *J. Comp. Chem.*, 18, 1463–1472.
36 Berendsen, H.J.C. *et al.* (1984) Molecular dynamics with coupling to an external bath. *J. Chem. Phys.*, 81, 3684–3690.
37. Bussi, G. *et al.* (2007) Canonical sampling through velocity rescaling. *J. Chem. Phys.*, 126, 014101.
38 Parrinello, M. *et al.* (1981) Polymorphic transitions in single crystals: a new molecular dynamics method. *J. Appl. Phys.*, 52, 7182–7190.
39. Kumari, R. *et al.*; Open Source Drug Discovery Consortium. (2014) g_mmpbsa – a GROMACS tool for high-throughput MM-PBSA calculations. *J. Chem. Inf. Model.*, 54, 1951–1962.
40. Paul, A.L. *et al.* (2012) 14-3-3 phosphoprotein interaction networks – does isoform diversity present functional interaction specification? *Front. Plant Sci.*, 3, 190.
41. Li, F. *et al.* (1998) Control of apoptosis and mitotic spindle checkpoint by survivin. *Nature*, 396, 580–584.
42. Tsang, T.J. *et al.* (2017) Subcellular localization of survivin determines its function in cardiomyocytes. *Theranostics*, 7, 4577–4590.
43. Ye, Q. *et al.* (2014) ERK and AKT signaling cooperate to translationally regulate survivin expression for metastatic progression of colorectal cancer. *Oncogene*, 33, 1828–1839.
44. Zhao, P. *et al.* (2010) Regulation of survivin by PI3K/Akt/p70S6K1 pathway. *Biochem. Biophys. Res. Commun.*, 395, 219–224.
45. Kohama, Y. *et al.* (2019) Regulation of the stability and activity of CDC25A and CDC25B by protein phosphatase PP2A and 14-3-3 binding. *Cell. Signal.*, 54, 10–16.
46. Pennington, K.L. *et al.* (2018) The dynamic and stress-adaptive signaling hub of 14-3-3: emerging mechanisms of regulation and context-dependent protein-protein interactions. *Oncogene*, 37, 5587–5604.
47. Chatterjee, D. *et al.* (2004) Reduction of 9-nitrocamptothecin-triggered apoptosis in DU-145 human prostate cancer cells by ectopic expression of 14-3-3zeta. *Int. J. Oncol.*, 25, 503–509.
48. Chuthapisith, S. *et al.* (2007) Proteomic profiling of MCF-7 breast cancer cells with chemoresistance to different types of anti-cancer drugs. *Int. J. Oncol.*, 30, 1545–1551.
49. Sinha, P. *et al.* (2000) Identification of novel proteins associated with the development of chemoresistance in malignant melanoma using two-dimensional electrophoresis. *Electrophoresis*, 21, 3048–3057.